

Ultrafast generation of hidden phases via energy-tuned electronic photoexcitation in magnetite

B. Truc, P. Usai, F. Pennacchio, G. Berruto, R. Claude, I. Madan,
T. LaGrange, G. M. Vanacore,* S. Benhabib,[†] and F. Carbone[‡]

Institute of Physics, LUMES, École Polytechnique Fédérale de Lausanne (EPFL), Lausanne CH-1015, Switzerland

V. Sala

Dipartimento di Fisica, Politecnico di Milano, Piazza Leonardo da Vinci 32, Milano, Italy

(Dated: October 4, 2022)

Metal-insulator transitions (MIT) occurring in non-adiabatic conditions can evolve through high-energy intermediate states that are difficult to observe and control via static methods. By monitoring the out-of-equilibrium structural dynamics of a magnetite (Fe_3O_4) crystal via ultrafast electron diffraction, we show that MITs can evolve through different pathways by properly selecting the electronic excitation with light. Near-infrared (800 nm) photons inducing d-d electronic transitions is found to favor the destruction of the long-range zigzag network of the trimerons and to generate a phase separation between cubic-metallic and monoclinic-insulating regions. Instead, visible light (400 nm) further promotes the long-range order of the trimerons by stabilizing the charge density wave fluctuations through the excitation of the oxygen 2p to iron 3d charge transfer and, thus, fosters a reinforcement of the monoclinic insulating phase. Our experiments demonstrate that tailored light pulses can drive strongly correlated materials into different hidden phases, influencing the lifetime and emergent properties of the intermediate states.

I. INTRODUCTION

The physical properties of strongly correlated materials are mainly defined by the complex interplay among the electronic, orbital, spin, and atomic degrees of freedom. At equilibrium, phase transitions follow an ergodic pathway within the material free-energy landscape, and the transition is characterized by a succession of thermodynamic equilibrium states between two global minima. Instead, using ultrashort laser pulses drive the transition out-of-equilibrium and induce a distinct pathway by transiently changing the coupling between the relevant degrees of freedom. Light-driven phase transitions reveal the presence of new intermediate (hidden) states of matter [1–9]. Such hidden phases are not only of interest from a fundamental point of view but also bear potential for ultrafast technological devices [9, 10].

Magnetite (Fe_3O_4) is a prototypical strongly-correlated system. It exhibits a complex interplay between the crystal structure [11], charge [12–15] and orbital orders [16, 17], which leads to the emergence of an atypical thermodynamic MIT in the vicinity of 125 K, known as the Verwey transition (VT) [18]. It is found that the structural changes play a key role in VT [19, 20]. Above Verwey temperature (T_V), magnetite has a cubic inverse spinel $Fd\bar{3}m$ structure formally written $\text{Fe}^{+3}[\text{Fe}^{+2}\text{Fe}^{+3}]\text{O}_4$, the first Fe^{+3} (A-type) occupied the tetrahedral sites, whereas the $[\text{Fe}^{+2}\text{Fe}^{+3}]$ (B-type) occupied the octahedral sites. Below the T_V , the symmetry

changes from the cubic $Fd\bar{3}m$ to the monoclinic Cc phase [11].

In the low-temperature (LT) phase, a new kind of bond dimerized state, the so-called trimeron, has been discovered and shown to form a long-range order [21, 22]. The trimeron unit results from multiple cooperative effects, including charge, t_{2g} orbital orderings, and strong electron-phonon coupling [23]. Therefore, trimerons are deemed to be the key actor of VT, which has been recently described microscopically as an order-disorder transition from a trimeron liquid with incommensurate fluctuations to a commensurate crystal below T_V [24–26]. Optical experiments have shown that light offers the intriguing possibility to manipulate such charge fluctuations resulting in tuning the electron-phonon coupling [26] and suggesting that the light-induced transition can be very orbital-selective. Here, we directly visualize the out-of-equilibrium structural dynamics of a magnetite single crystal employing ultrafast electron diffraction (UED).

UED allows us to track the lattice evolution of magnetite across the photoinduced MIT. We show that, depending on the photon energy of the femtosecond optical excitation used in the experiment (1.55 eV vs. 3.10 eV), we trigger different electronic excitations, consequently leading to distinct nonequilibrium metastable structural states.

II. EXPERIMENTAL METHODS

The UED experiments were performed in reflection geometry [27, 28] with a grazing angle of 0.5° to 5° . The light source is a Ti:sapphire laser amplifier with a central wavelength of 800 nm with a pulse duration of 45 fs at a repetition rate of 20 kHz.

* Currently at Department of Materials Science, LUMiNaD, University of Milano-Bicocca, Via Cozzi 55, 20125 Milan, Italy

[†] siham.benhabib@epfl.ch

[‡] fabrizio.carbone@epfl.ch

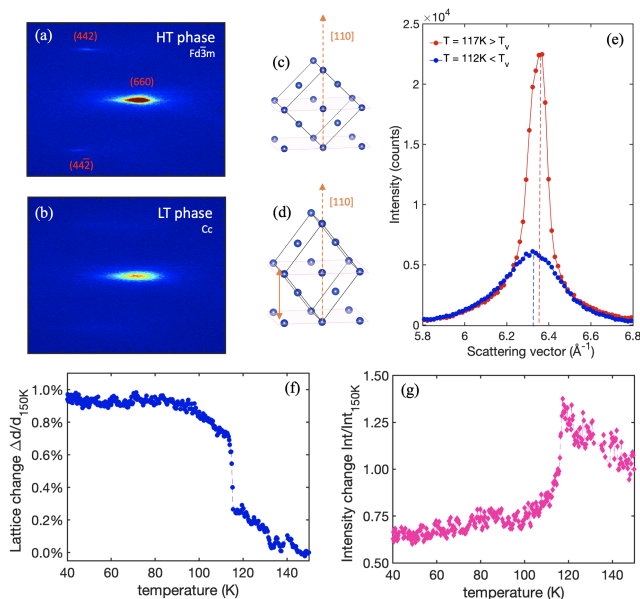


FIG. 1. Static diffraction pattern of magnetite in the cubic phase $Fd\bar{3}m$ above T_V , $T=150$ K (a) and in the monoclinic phase Cc below T_V at $T=40$ K (b). (c) Cubic face-centered structure oriented along the $[110]$ direction reflecting the cubic unit cell of magnetite above T_V . (d) The elongated unit cell of magnetite below T_V . (e) Peak profile of the (660) Bragg peak above and below T_V , its parameters are extracted from a Voigt profile fit. (f) Temperature dependence of the interplanar atomic change (expansion/compression) along $[110]$ extracted from the (660) Bragg peak position (see SI). (h) Evolution of the integrated area under the (660) Bragg peak across the transition.

High-quality magnetite with $T_V \approx 117$ K exposing the flat and optically polished (110) surface was fixed on a cold finger attached to a five-axis manipulator with silver conductive paste and placed inside an ultrahigh vacuum chamber ($\leq 10^{-9}$ mbar). The temperature range is controlled using an open cycle cryostat with helium liquid flow (see the SI).

III. RESULTS

We have first monitored the quasi-adiabatic transition induced by varying the temperature of magnetite (without photoexcitation). We investigate the structural changes by decreasing the temperature from 150 K down to 40 K and simultaneously following the quasi-static change of the diffraction pattern along the $[110]$ direction where anomalies attributed to the trimerons have been recently observed [29].

In Fig.1(a) and (b), we show the static diffraction patterns of magnetite measured above and below T_V , respectively. Specifically, we monitor the changes of the (660) Bragg peak of the cubic phase and observe a significant modification of the peak position from which we extract the atomic interplanar expansion or compression

(see SI) shown in Fig.1(f). This is accompanied by a drop in the diffraction intensity as illustrated in Fig.1(g). Such intensity drop results from the combination of two concomitant factors: i) the lowering of the structure factor when transitioning from a high-symmetry cubic phase to a lower symmetry monoclinic structure, and ii) the incoherent electron scattering process through multiple micro-sized structural domains (twins) that emerge in LT phase [30]. Across VT, at 117 K, the cubic lattice transforms into the monoclinic phase, which is evidenced by the expansion of the lattice along the $[110]$ direction, as sketched in Fig.1(d). This specific expansion significantly changes the shear strain ε_{xy} (see SI). In addition, it causes a significant softening in the shear elastic constant c_{44} , as reported in ultrasound measurements [31]. Although our technique is moderately surface sensitive (5-10 nm), the agreement between the monitored position shift of the Bragg peak from our data and the reported softening in the elastic constant c_{44} demonstrates that our observations are representative of bulk dynamics.

Ginzburg-Landau's (GL) theory of phase transition such as VT in magnetite correlates transformation shear strains to an order parameter. Hence, we ascribe the measured shear strain (ε_{xy}) being strongly coupled to the order parameter (OP) Δ , and retrieve its symmetry based on the framework of GL [32] and a fundamental group theory analysis (see SI). We found that Δ has T_{2g} symmetry with one nonzero component, i.e., $\Delta = (\Delta_{xy}, 0, 0)$.

Using detailed group theory calculations, several authors have identified the set of phonons, including Δ_5 , X_3 , and Γ^{+5} (T_{2g}), as the structural OPs [33–35]. Furthermore, *ab initio* calculations have demonstrated the strong coupling between these structural OPs and the T_{2g} orbital ordering within a trimeron [33]. Therefore, we conclude that the trimerons arrangement along the $[110]$ direction is a conceivable OP candidate with T_{2g} representation. The OP with T_{2g} representation was suggested recently by electron diffraction measurements, where the authors consider an anomalous electronic nematic phase above T_V with a T_{2g} representation which involves a different set of rotational symmetry breaking than the usual ones [36].

We obtain insights into the non-adiabatic MIT in magnetite by investigating the out-of-equilibrium response of the lattice, initially kept at 80 K (below T_V), after photoexcitation. In Fig.2, we present the evolution of the (660) Bragg peak following ultrashort laser pulses at two different wavelengths, 800 nm and 400 nm at 2.9 mJ/cm² and 1.2 mJ/cm² incident fluence, respectively. The fluence used for 800 nm corresponds to the *intermediate* fluence regime [37].

Fig.2(a) shows the structural dynamics following 800 nm photoexcitation. The (660) atomic planes undergo a maximum compression of around -0.06%. Based on our static data shown above (Fig.1), the compression of the monoclinic lattice along the $[110]$ direction denotes the transformation toward a cubic structure, con-

sistent with ref.[37]. Their recent out-of-equilibrium optical measurements have shown a photoinduced phase separation between insulating regions and metallic islands at LT through 800 nm laser pulses in a similar fluence regime. This observation is supported by pump-probe x-ray diffraction measurements [38], where the authors attribute the insulating state to the monoclinic regions and the metallic state to the cubic islands. Expanding the investigation range of previous measurements that were limited to the first 10 ps [36–38], our data unveil the complex establishment of the hidden phase which lasts approximately 50 ps and interestingly follows three compression stages. First, during the first 22 ps (N°1), an abrupt compression of -0.03% occurs. In the second stage (N°2) between 22 ps and 27 ps, the lattice undergoes a minor contraction. Finally, the third step (N°3) emerges and adds an extra -0.03% to the lattice compression. This multi-step process is characteristic of the presence of distinct dynamic processes, such as electron-phonon coupling and phonon-phonon interaction [36, 39]. Note that the electron-electron interaction is expected to occur on a faster timescale < 300 fs [38], beyond the temporal resolution in these experiments. The relaxation process also evolves with multiple timescales. Qualitatively, the first recovery stage (N°4) occurs from 50 ps to 126 ps and reaches an intermediate compressed state close to -0.03%, which interestingly corresponds to the value of the process N°3. Then, a second long process occurs towards the total recovery (N°5) to the equilibrium phase, which is still not reached after 1.3 ns (see SI). In a second data set with a slightly higher fluence (see SI), we confirm the multiple compression stage process and show that each stage’s duration and amplitude depend on the fluence used.

In Fig.2(c), the response of the Bragg peak intensity after the 800 nm photoexcitation shows a drop. Taking only into account the recovery towards the higher symmetry cubic high temperature phase after the 800 nm photoexcitation, we expect an increase in the intensity, which we do not observe. This observation suggests that the dominant process is the structural disorder caused by the motion of the atoms induced by the rise in the lattice temperature by ultrashort laser pulses [40], known as the induced Debye-Waller effect (see SI). Similarly to the peak position shift response, the Bragg peak intensity does not fully recover to its initial state after 1.3 ns (see SI). The long dynamics revealed by our data indicate the metastability of the induced 800 nm phase illustrating the complexity of the thermalization process in magnetite, involving multiple interplays of electron-electron, electron-phonon, and phonon-phonon scattering. Such lifetime is a signature of a hidden out-of-equilibrium phase which is supported by the unusual structural dynamics and the decrease in the intensity due to the phase separation between cubic and monoclinic islands, which is not an equilibrium state but rather a local minimum within the energy landscape of the excited configuration.

We extend our investigation for hidden phases in mag-

netite by changing the energy of the optical excitation to 3.10 eV (400 nm). In Fig.2(b), different from the 800 nm case, we observe that the 400 nm laser pulses induce a 0.4% expansion of the lattice along the [110] direction (instead of a contraction), indicating a reinforcement of the monoclinic distortion. At 90 K, before excitation, the crystalline structure has a monoclinic angle $\beta_M = 90.236^\circ$ [21]. The 400 nm induced expansion is mainly related to the variation of the tilting angle β_M , where we expect a value $\beta_{M400\text{ nm}} > 90.236^\circ$. A quantitative value for the tilting angle can only be retrieved when monitoring the behavior of multiple Bragg peaks along different zone axes. Nevertheless, our data clearly show that the 400 nm optical excitation induces a lattice change that is opposite to the quasi-adiabatic lattice response from our equilibrium data presented above (Fig.1(f)), where the stabilization of the structure from 90 K down to 40 K shows no modification of the lattice parameters expected thermodynamically. Since the generated structure is not accessible thermally but only induced optically, we associate it with the emergence of a new hidden phase characterized by a monoclinic lattice with a tilting angle larger than the equilibrium value of 90.236° . The 400 nm hidden phase is also completely different from the one established by the 800 nm light. The first is firmly monoclinic, whereas the second is a mixture of monoclinic and cubic separated regions. The 400 nm structural hidden phase takes around 50 ps to emerge with only one direct expansion process, as presented in Fig.2(b), which we relate mainly to electron-phonon interaction. This new state lasts up to 300 ps without any recovery to the initial state giving it a metastable character. We observe a significant drop in the intensity response (Fig.2(d)). For the 800 nm case, thermal effects and multiple scatterings from the mixed phase are the origins of the intensity drop. Although the decrease in intensity is consistent with the reduction of the structure factor for the (660) Bragg peak, it is surprising to observe a shrinking of the FWHM, indicating a higher homogeneity in the atomic planes, which we cannot associate with a thermal-like behavior. This suggests that the new hidden structural state possesses a larger structural long-range order related to a larger monoclinic angle.

IV. DISCUSSION

The formation of distinct metastable hidden phases through two different photon energies demonstrates the critical role played by electronic excitations in establishing such nonequilibrium phases in magnetite. At LT, magnetite is thermodynamically stabilized in the insulating phase, resulting from a commensurate long-range order along the [001] direction [21, 38] of the trimerons zigzag network [22, 41] with a coherent length of (385 ± 10) nm [14]. Each trimeron unit couples linearly three Fe_B sites in the form $\text{Fe}_B^{3+} - \text{Fe}_B^{2+} - \text{Fe}_B^{3+}$, in which the minority spin t_{2g} electron is delocalized from

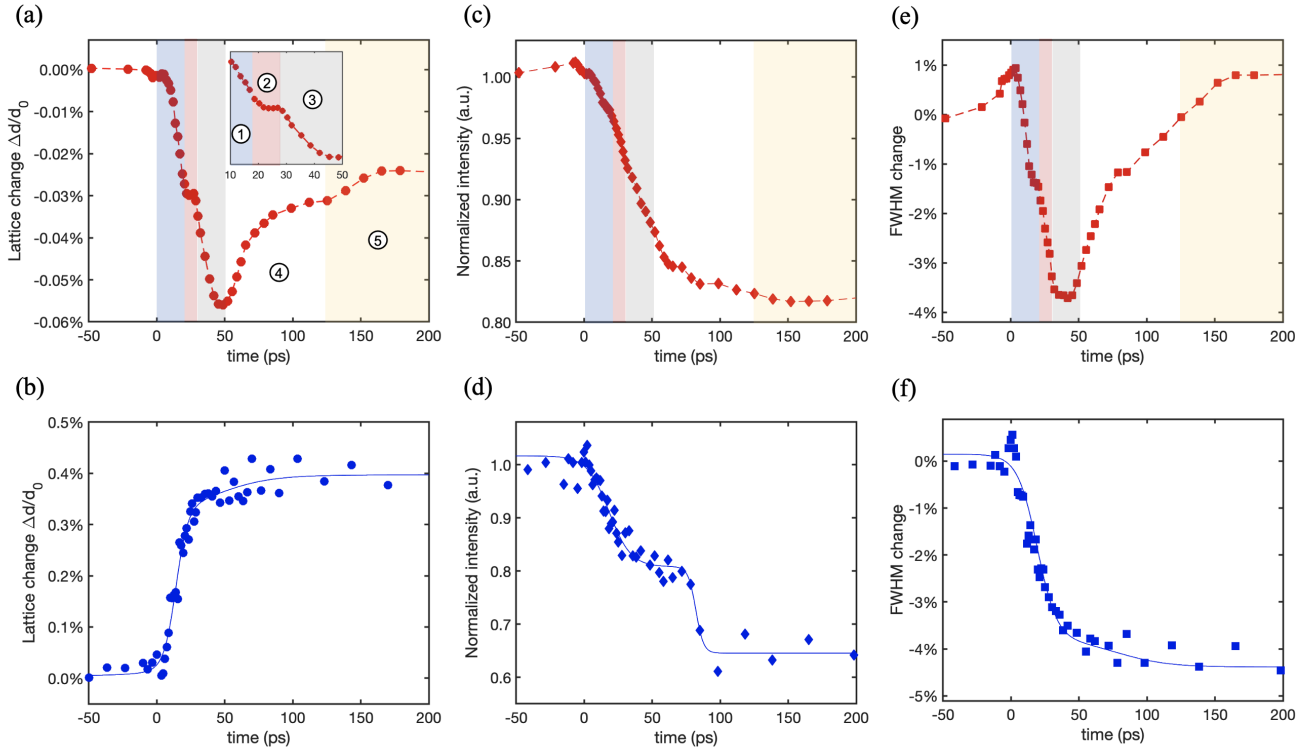


FIG. 2. Evolution of the lattice change compression/expansion along the [110] direction (a) under 800 nm and (b) 400 nm photoexcitation. In (a), the shaded areas show multiple compression stages. (c) and (d) evolution of the normalized intensity under 800 nm and 400 nm photoexcitation, respectively. (e) and (f) time dependence of the FWHM (full width at half maximum) under 800 nm and 400 nm photoexcitation, respectively. Solid lines are guides to the eye.

the central Fe_B^{2+} site into the nearest neighbors Fe_B^{3+} , and each Fe_B^{3+} site is shared between three trimeron. In addition to the Jahn-Teller distortion caused by the orbital ordering [42], the electron localization within a trimeron unit produces a structural distortion in the Fe_B sites, where the distance between the central Fe_B^{2+} and its two Fe_B^{3+} nearest neighbors gets shorter, leading to a monoclinic distortion [21]. This distortion has been confirmed by high-accuracy synchrotron x-ray structure refinements [43], where it is found that fourteen over the sixteen nonequivalent trimeron units have shown a shorter $\text{Fe}_B - \text{Fe}_B$ distance. When we excite magnetite using photon pulses with an energy of 1.55 eV (800 nm), LDA+U calculations [16] and optical conductivity measurements [37, 44] both agree in predicting the triggering of electronic d-d excitations. They correspond to an electron delocalization from an occupied t_{2g} of Fe_B^{2+} to an unoccupied t_{2g} orbital of Fe_B^{3+} following the configuration $3d_7^6 3d_j^5 \rightarrow 3d_i^5 3d_j^6$. The d-d excitations encompass another inter-site excitation corresponding to the transition from an occupied t_{2g} of Fe_B^{2+} to an unoccupied e_g of Fe_B^{3+} [16]. However, this excitation is only possible at an energy higher than 2 eV. Triggering the d-d excitation restores the mobility of the minority spin t_{2g} electrons and causes the valency to change for both Fe_B^{2+} and Fe_B^{3+} and, hence, alternates their sites inside the trimeron (see SI).

The direct consequence of this local electronic fluctuation is the destruction of the trimeron. According to out-of-equilibrium x-rays measurements, this destruction occurs in an ultrashort timescale < 300 fs [38]. The destruction of trimeron yields the suppression of the long-range zigzag order connected at Fe_B^{3+} sites. When the trimeron breaks, the $\text{Fe}_B - \text{Fe}_B$ distance returns to its initial value. Hence, the structure relaxes, giving rise to the emergence of cubic phase islands inside the remaining monoclinic regions forming a phase separation that we qualify as an 800 nm metastable hidden phase. Following the electronic excitation, the relaxation process back to the equilibrium configuration continues via electron-phonon and phonon-phonon scattering mechanisms. Electrons primarily interact with high-energy optical phonons, which then anharmonically decay toward acoustic modes via a three-phonon scattering process [45–48]. For magnetite, we can interpret the newly observed two steps in the relaxation process as the strong electron-phonon coupling involving the conduction electrons coupling with the X_3 -driven mode (TO) for the first stage and the phonon-phonon coupling between X_3 (TO) and Δ_5 (TA) modes for the second. This scenario is supported by recent UED data that have shown under similar photoexcitation (800 nm) that the X_3 (TO) mode is preferably triggered via the electron-phonon coupling [36] in the first few pi-

coseconds. In addition, inelastic neutron scattering has shown that the Δ_5 (TA) mode is the most susceptible across the cubic-monoclinic transformation [24].

In the equilibrium state, refined x-rays measurements show that in a high connectivity configuration with a maximum of three trimers per Fe_B^{3+} site, only four of the eight Fe_B^{3+} sites participate, keeping the rest as inactive [21]. In addition, our static data in Fig.1 show that this thermodynamic maximum connectivity state is reached a few kelvins after T_V , and no extra monoclinic distortion is observed from 90 K down to 40 K. When we excite the magnetite crystal with the 400 nm (3.10 eV) light, we trigger multiple electronic excitations (see SI). The most dominant excitation is the charge transfer from 2p bands of oxygen to 3d bands of Fe_B [44]. By activating the ligand-metal charge transfer, the oxygens of the octahedron FeO_6 supply electrons to the Fe_B^{3+} non-participating ions, which consequently become Fe_B^{2+} . Hence, the proportion of Fe_B^{2+} increases at the inactive trimers B-sites, boosting t_{2g} orbital ordering and creating extra trimers, thus pushing beyond the limit of the thermodynamic maximum connectivity state leading to a new light-induced phase. This causes additional stress on the magnetite structure provoked by cooperative effects. One is the Jahn-Teller distortion due to the extending t_{2g} orbital ordering. At the same time, the second contribution comes from the shortening of the atomic $\text{Fe}_B - \text{Fe}_B$ distances induced by the charge localization within the newly formed trimers (charge ordering) [21, 43]. Recently, a high-accuracy x-ray experiment has shown that chemically doped magnetite introduces B site-selective Fe^{2+} vacancies (which become Fe^{3+}) and weakens the trimeron long range order [49]. The authors attribute the vanishing of the VT in doped magnetite to the absence of the trimeron network. In our case, the 400 nm photo-doping acts oppositely and provides additional electrons to the incomplete trimeron network. As our data clearly shows, this results in an expansion of the lattice along the [110] direction. It is reasonable to speculate that the photo-doping is site-selective, which

orders and strengthens the trimeron crystal seen in the increase of the coherence length (Fig.2(f)). In this scenario, the trimeron network can be seen as an imperfect Wigner crystal with homogeneous vacancies (inactive Fe^{3+} B-sites). After 400 nm photo-doping, the electrons from the oxygens activate the missing sites and complete the trimeron crystal enhancing the connectivity, which ultimately induces a monoclinic distortion favored by a strong electron-phonon coupling.

V. CONCLUSION

Our results reveal the emergence of two distinct metastable hidden phases in magnetite. Starting from the same LT equilibrium state, we drive magnetite into two different structural states using two different photon energies. The 800 nm light induces d-d excitations, which favor the destruction of the trimers and their network in a percolating fashion, leading to a phase separation between monoclinic-insulating regions and cubic-metallic islands. The 400 nm light triggers charge transfer between oxygen and iron at B-sites, which are found to be prolific for the trimers and their arrangement, enhancing their connectivity, which leads to a stronger monoclinic distortion inaccessible adiabatically. Our findings demonstrate the key role of the trimeron structural configuration in magnetite and show the ability to establish novel hidden phases in quantum materials via specific electronic excitations in a strongly correlated environment.

ACKNOWLEDGMENTS

The authors are grateful to J. Lorenzana, W. Tabis, A. Kozłowski and P. Piekarczyk for constructive discussions. This work was supported by the ERC consolidator grant ISCQuM No. 771346, SNSF grant No.514725, NCCR-MUST No. 565194.

-
- [1] D Fausti, R I Tobey, N Dean, S Kaiser, A Dienst, M C Hoffmann, S Pyon, T Takayama, H Takagi, and A Cavalleri. Light-Induced Superconductivity in a Stripe-Ordered Cuprate. *Science*, 331(6014):189–191, jan 2011.
- [2] V. Kiryukhin, D. Casa, J. P. Hill, B. Keimer, A. Vigliante, Y. Tomioka, and Y. Tokura. An X-ray-induced insulator–metal transition in a magnetoresistive manganite. *Nature*, 386(6627):813–815, apr 1997.
- [3] L. Stojchevska, I. Vaskivskiy, T. Mertelj, P. Kusar, D. Svetin, S. Brazovskii, and D. Mihailovic. Ultrafast switching to a stable hidden quantum state in an electronic crystal. *Science*, 344(6180):177–180, 2014.
- [4] K. Miyano, T. Tanaka, Y. Tomioka, and Y. Tokura. Photoinduced Insulator-to-Metal Transition in a Perovskite Manganite. *Physical Review Letters*, 78(22):4257–4260, jun 1997.
- [5] Hirohiko Ichikawa, Shunsuke Nozawa, Tokushi Sato, Ayana Tomita, Kouhei Ichiyangi, Matthieu Chollet, Laurent Guerin, Nicky Dean, Andrea Cavalleri, Shin-ichi Adachi, Taka-hisa Arima, Hiroshi Sawa, Yasushi Ogi-moto, Masao Nakamura, Ryo Tamaki, Kenjiro Miyano, and Shin-ya Koshihara. Transient photoinduced ‘hidden’ phase in a manganite. *Nature Materials*, 10(2):101–105, feb 2011.
- [6] Frank Y. Gao, Zhuquan Zhang, Zhiyuan Sun, Linda Ye, Yu-Hsiang Cheng, Zi-Jie Liu, Joseph G. Checkelsky, Edoardo Baldini, and Keith A. Nelson. Snapshots of a light-induced metastable hidden phase driven by the collapse of charge order. *Science Advances*, 8(29):1–12, jul 2022.

- [7] Abdolnasser Zakery and Stephen R. Elliott. *Optical Non-linearities in Chalcogenide Glasses and Their Applications*, chapter CHAPTER 14, pages 433–486. 2021.
- [8] S. Koshihara, Y. Tokura, T. Mitani, G Saito, and T. Koda. Photoinduced valence instability in the organic molecular compound tetrathiafulvalene-*p*-chloranil (TTF-CA). *Physical Review B*, 42(10):6853–6856, oct 1990.
- [9] Alberto de la Torre, Dante M. Kennes, Martin Claassen, Simon Gerber, James W. McIver, and Michael A. Sentef. Colloquium: Nonthermal pathways to ultrafast control in quantum materials. *Reviews of Modern Physics*, 93(4):041002, oct 2021.
- [10] Feliciano Giustino, Jin Hong Lee, Felix Trier, Manuel Bibes, Stephen M Winter, Roser Valentí, Young-woo Son, Louis Taillefer, Christoph Heil, Adriana I Figueroa, Bernard Plaçons, Quansheng Wu, Oleg V Yazev, Erik P A M Bakkers, Jesper Nygård, Pol Forn-Díaz, Silvano De Franceschi, J W McIver, L E F Foa Torres, Tony Low, Anshuman Kumar, Regina Galceran, Sergio O Valenzuela, Marius V Costache, Aurélien Manchon, Eun-Ah Kim, Gabriel R Schleder, Adalberto Fazzio, and Stephan Roche. The 2021 quantum materials roadmap. *Journal of Physics: Materials*, 3(4):042006, oct 2020.
- [11] M. Iizumi, T. F. Koetzle, G. Shirane, S. Chikazumi, M. Matsui, and S. Todo. Structure of magnetite (Fe₃O₄) below the Verwey transition temperature. *Acta Crystallographica Section B Structural Crystallography and Crystal Chemistry*, 38(8):2121–2133, aug 1982.
- [12] E. Nazarenko, J. E. Lorenzo, Y. Joly, J. L. Hodeau, D. Mannix, and C. Marin. Resonant X-Ray Diffraction Studies on the Charge Ordering in Magnetite. *Physical Review Letters*, 97(5):056403, aug 2006.
- [13] Richard J. Goff, Jon P. Wright, J. Paul Attfield, and Paolo G. Radaelli. Resonant x-ray diffraction study of the charge ordering in magnetite. *Journal of Physics: Condensed Matter*, 17(48):7633–7642, dec 2005.
- [14] J. E. Lorenzo, C. Mazzoli, N. Jaouen, C. Detlefs, D. Mannix, S. Grenier, Y. Joly, and C. Marin. Charge and Orbital Correlations at and above the Verwey Phase Transition in Magnetite. *Physical Review Letters*, 101(22):226401, nov 2008.
- [15] J. P. Wright, J. P. Attfield, and P. G. Radaelli. Long Range Charge Ordering in Magnetite Below the Verwey Transition. *Physical Review Letters*, 87(26):266401, dec 2001.
- [16] I. Leonov, A. N. Yaresko, V. N. Antonov, M. A. Korotin, and V. I. Anisimov. Charge and Orbital Order in Fe₃O₄. *Physical Review Letters*, 93(14):146404, sep 2004.
- [17] Horng-Tay Jeng, G. Y. Guo, and D. J. Huang. Charge-Orbital Ordering and Verwey Transition in Magnetite. *Physical Review Letters*, 93(15):156403, oct 2004.
- [18] E. J. W. Verwey. Electronic Conduction of Magnetite (Fe₃O₄) and its Transition Point at Low Temperatures. *Nature*, 144(3642):327–328, aug 1939.
- [19] D Ihle and B Lorenz. Electron correlation theory of Fe₃O₄. *Philosophical Magazine B*, 42(3):337–347, sep 1980.
- [20] Y. Yamada. Charge ordering and lattice instability in magnetite. *AIP Conference Proceedings*, 24(1):79–85, 1975.
- [21] Mark S. Senn, Jon P. Wright, and J. Paul Attfield. Charge order and three-site distortions in the Verwey structure of magnetite. *Nature*, 481(7380):173–176, jan 2012.
- [22] Mark S. Senn, Ingo Loa, Jon P. Wright, and J. Paul Attfield. Electronic orders in the Verwey structure of magnetite. *Physical Review B*, 85(12):125119, mar 2012.
- [23] Przemysław Piekarczyk, Dominik Legut, Edoardo Baldini, Carina A. Belvin, Tomasz Kołodziej, Wojciech Tabiś, Andrzej Kozłowski, Zbigniew Kakol, Zbigniew Tarnawski, José Lorenzana, Nuh Gedik, Andrzej M. Oleś, Jürgen M. Honig, and Krzysztof Parlinski. Trimeron-phonon coupling in magnetite. *Physical Review B*, 103(10):104303, mar 2021.
- [24] S. Borroni, G. S. Tucker, F. Pennacchio, J. Rajeswari, U. Stuhr, A. Pisoni, J. Lorenzana, H M Rønnow, and F. Carbone. Mapping the lattice dynamical anomaly of the order parameters across the Verwey transition in magnetite. *New Journal of Physics*, 19(10):103013, oct 2017.
- [25] S. Borroni, G. S. Tucker, U. Stuhr, J. Lorenzana, H. M. Rønnow, and F. Carbone. Energy domain versus time domain precursor fluctuations above the Verwey transition in magnetite. *Physical Review B*, 101(5):054303, feb 2020.
- [26] S. Borroni, E. Baldini, V. M. Katukuri, A. Mann, K. Parlinski, D. Legut, C. Arrell, F. van Mourik, J. Teyssier, A. Kozłowski, P. Piekarczyk, O. V. Yazev, A. M. Oleś, J. Lorenzana, and F. Carbone. Coherent generation of symmetry-forbidden phonons by light-induced electron-phonon interactions in magnetite. *Physical Review B*, 96(10):104308, sep 2017.
- [27] Giulia Fulvia Mancini, Barbara Mansart, Saverio Pagano, Bas van der Geer, Marieke de Loos, and Fabrizio Carbone. Design and implementation of a flexible beamline for fs electron diffraction experiments. *Nuclear Instruments and Methods in Physics Research Section A: Accelerators, Spectrometers, Detectors and Associated Equipment*, 691:113–122, nov 2012.
- [28] Francesco Pennacchio, Giovanni M. Vanacore, Giulia F. Mancini, Malte Oppermann, Rajeswari Jayaraman, Pietro Musumeci, Peter Baum, and Fabrizio Carbone. Design and implementation of an optimal laser pulse front tilting scheme for ultrafast electron diffraction in reflection geometry with high temporal resolution. *Structural Dynamics*, 4(4):044032, jul 2017.
- [29] Jung-Fu Lin, Junjie Wu, Jie Zhu, Zhu Mao, Ayman H. Said, Bogdan M. Leu, Jinguang Cheng, Yoshiya Uwatoko, Changqing Jin, and Jianshi Zhou. Abnormal Elastic and Vibrational Behaviors of Magnetite at High Pressures. *Scientific Reports*, 4(1):6282, may 2015.
- [30] Takeshi Kasama, Nathan S. Church, Joshua M. Feinberg, Rafal E. Dunin-Borkowski, and Richard J. Harrison. Direct observation of ferrimagnetic/ferroelastic domain interactions in magnetite below the Verwey transition. *Earth and Planetary Science Letters*, 297(1-2):10–17, aug 2010.
- [31] H. Schwenk, S. Bareiter, C. Hinkel, B. Lüthi, Z. Kakol, A. Kosłowski, and J.M. Honig. Charge ordering and elastic constants in Fe Zn O. *The European Physical Journal B*, 13(3):491–494, jan 2000.
- [32] L D Landau and E. M Lifschitz. *Statistical Physics*. Butterworth-Heinemann, third edit edition, 1980.
- [33] Przemysław Piekarczyk, Krzysztof Parlinski, and Andrzej M. Oleś. Origin of the Verwey transition in magnetite: Group theory, electronic structure, and lattice dynamics study. *Physical Review B*, 76(16):165124, oct 2007.

- [34] L. V. Gasparov, D. B. Tanner, D. B. Romero, H. Berger, G. Margaritondo, and L. Forró. Infrared and Raman studies of the Verwey transition in magnetite. *Physical Review B*, 62(12):7939–7944, sep 2000.
- [35] Przemysław Piekarczyk, Krzysztof Parlinski, and Andrzej M. Oleś. Mechanism of the Verwey Transition in Magnetite. *Physical Review Letters*, 97(15):156402, oct 2006.
- [36] Wei Wang, Jun Li, Zhixiu Liang, Lijun Wu, Pedro M. Lozano, Alexander C. Komarek, Xiaozhe Shen, Alex H. Reid, Xijie Wang, Qiang Li, Weiguo Yin, Kai Sun, Yimei Zhu, Ian K. Robinson, Mark P. M. Dean, and Jing Tao. Verwey transition as evolution from electronic nematicity to trimerons via electron-phonon coupling. *arxiv.org/2202.08744*, feb 2022.
- [37] F. Randi, I. Vergara, F. Novelli, M. Esposito, M. Dell’Angela, V. A. M. Brabers, P. Metcalf, R. Kukreja, H. A. Dürr, Daniele Fausti, M. Grüninger, and F. Parmigiani. Phase separation in the nonequilibrium Verwey transition in magnetite. *Physical Review B*, 93(5):054305, feb 2016.
- [38] S. de Jong, R. Kukreja, C. Trabant, N. Pontius, C. F. Chang, T. Kachel, M. Beye, F. Sorgenfrei, C. H. Back, B. Bräuer, W. F. Schlotter, J. J. Turner, O. Krupin, M. Doehler, D. Zhu, M. A. Hossain, A. O. Scherz, D. Fausti, F. Novelli, M. Esposito, W. S. Lee, Y. D. Chuang, D. H. Lu, R. G. Moore, M. Yi, M. Trigo, P. Kirchmann, L. Pathey, M. S. Golden, M. Buchholz, P. Metcalf, F. Parmigiani, W. Wurth, A. Föhlisch, C. Schüßler-Langeheine, and H. A. Dürr. Speed limit of the insulator–metal transition in magnetite. *Nature Materials*, 12(10):882–886, oct 2013.
- [39] Pablo Maldonado, Karel Carva, Martina Flammer, and Peter M. Oppeneer. Theory of out-of-equilibrium ultrafast relaxation dynamics in metals. *Physical Review B*, 96(17):174439, nov 2017.
- [40] Gustaaf Van.Tendeloo. 4D Electron Microscopy Imaging in Space and Time, By Ahmed.H. Zewail and John.M. Thomas. *Angewandte Chemie International Edition*, 50(13):2888–2888, 2011.
- [41] R. Řezníček, V. Chlan, H. Štěpánková, and P. Novák. Hyperfine field and electronic structure of magnetite below the Verwey transition. *Physical Review B*, 91(12):125134, mar 2015.
- [42] H. Y. Huang, Z. Y. Chen, R. P. Wang, F. M. F. de Groot, W. B. Wu, J. Okamoto, A. Chainani, A. Singh, Z. Y. Li, J. S. Zhou, H. T. Jeng, G. Y. Guo, Je-Geun Park, L. H. Tjeng, C. T. Chen, and D. J. Huang. Jahn-Teller distortion driven magnetic polarons in magnetite. *Nature Communications*, 8(1):15929, aug 2017.
- [43] Mark S. Senn, Jon P. Wright, James Cumby, and J. Paul Attfield. Charge localization in the Verwey structure of magnetite. *Physical Review B*, 92(2):024104, jul 2015.
- [44] S. K. Park, T. Ishikawa, and Y. Tokura. Charge-gap formation upon the Verwey transition in Fe₃O₄. *Physical Review B*, 58(7):3717–3720, aug 1998.
- [45] L. Perfetti, P. A. Loukakos, M. Lisowski, U. Bovensiepen, H. Eisaki, and M. Wolf. Ultrafast Electron Relaxation in Superconducting Bi₂Sr₂CaCu₂O_{8+δ} by Time-Resolved Photoelectron Spectroscopy. *Physical Review Letters*, 99(19):197001, nov 2007.
- [46] Fabrizio Carbone, Ding-Shyue Yang, Enrico Giannini, and Ahmed H. Zewail. Direct role of structural dynamics in electron-lattice coupling of superconducting cuprates. *Proceedings of the National Academy of Sciences*, 105(51):20161–20166, dec 2008.
- [47] Barbara Mansart, José Lorenzana, Andreas Mann, Ahmad Odeh, Mariateresa Scarongella, Majed Chergui, and Fabrizio Carbone. Coupling of a high-energy excitation to superconducting quasiparticles in a cuprate from coherent charge fluctuation spectroscopy. *Proceedings of the National Academy of Sciences*, 110(12):4539–4544, mar 2013.
- [48] Barbara Mansart, Mathieu J. G. Cottet, Thomas J. Penfold, Stephen B. Dugdale, Riccardo Tediosi, Majed Chergui, and Fabrizio Carbone. Evidence for a Peierls phase-transition in a three-dimensional multiple charge-density waves solid. *Proceedings of the National Academy of Sciences*, 109(15):5603–5608, apr 2012.
- [49] E. Pachoud, J. Cumby, G. Perversi, J. P. Wright, and J. P. Attfield. Site-selective doping of ordered charge states in magnetite. *Nature Communications*, 11(1):1671, dec 2020.

Supplemental Material: Ultrafast generation of hidden phases via energy-tuned electronic photoexcitation in magnetite

B. Truc, P. Usai, F. Pennacchio, G. Berruto, R. Claude, I. Madan,
T. LaGrange, G. M. Vanacore,* S. Benhabib,[†] and F. Carbone[‡]

Institute of Physics, LUMES, École Polytechnique Fédérale de Lausanne (EPFL), Lausanne CH-1015, Switzerland

V. Sala

Dipartimento di Fisica, Politecnico di Milano, Piazza Leonardo da Vinci 32, Milano, Italy

(Dated: October 4, 2022)

I. EXPERIMENTAL METHOD

The diffraction patterns are obtained using time-resolved high-energy electron diffraction in a reflection geometry (tr-RHEED, Fig.1), with a grazing angle of 0.5° to 5° . The light source is a Ti:sapphire laser with a central wavelength of 800 nm with a pulse duration of 45 fs at a repetition rate of 20 kHz. The beam is split into two optical paths, one for the pump (light-excitation) and the second for the probe. To generate the electrons, the third harmonic generation process is used to obtain UV of a wavelength of 266 nm, which illuminates a silver-coated sapphire photocathode. The emitted electrons, around 10^5 - 10^6 electrons per pulse, are accelerated with a high voltage of 30 keV. To overcome the space-charge effect [1], a 3 GHz radiofrequency cavity temporally compresses the electron beam. The setup is combined with a designed optimal laser front tilting scheme to correct the velocity mismatch between the optical pump and the electrons at the sample surface, allowing an overall temporal resolution of ≈ 500 fs [2]. Data were collected using two different cameras, PI-MAX 1300 Princeton Charge-Coupled Device with a number of pixels of 1340×1300 , with a pixel size of $20 \times 20 \mu\text{m}^2$ combined with a microchannel plate and a direct electron (QUADRO-DECTRIS) with a resolution of 514×514 with a pixel size of $75 \times 75 \mu\text{m}^2$. The sample was fixed on a cold finger attached to a five-axis manipulator

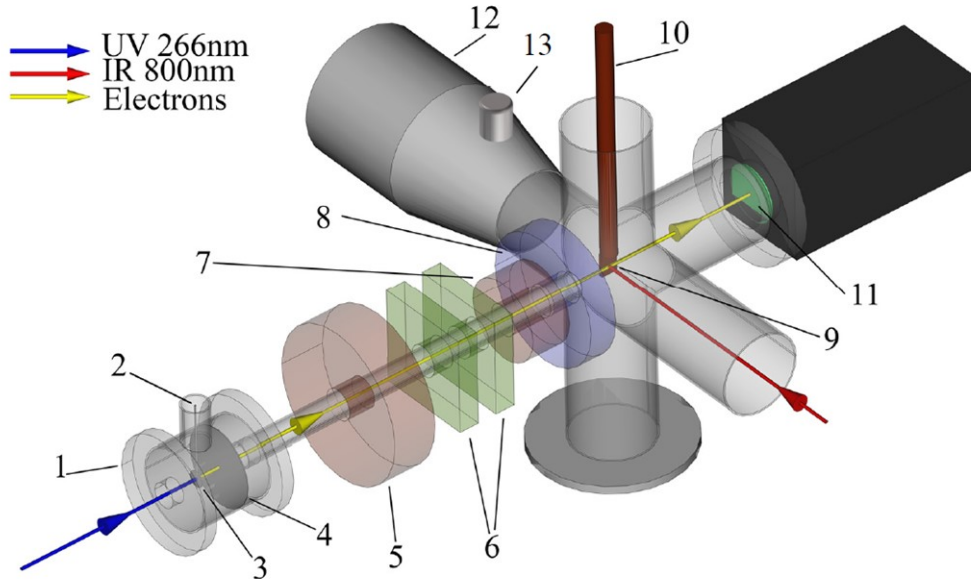


FIG. 1. Sketch of the UED setup at EPFL, 1) Electron gun, 2) HV connector, 3) Photocathode, 4) Anode, 5) Collimating solenoid, 6) Steering plates, 7) Focusing solenoid, 8) RF cavity, 9) Sample holder, 10) Cryostat, 11) Electron detector, 12) Ion pump, 13) Ion gauge

* Currently at Department of Materials Science, LUMiNaD, University of Milano-Bicocca, Via Cozzi 55, 20125 Milan, Italy

[†] siham.benhabib@epfl.ch

[‡] fabrizio.carbone@epfl.ch

with silver conductive paste and placed inside an ultra-high vacuum chamber ($\leq 10^{-9}$ mbar). The temperature range is controlled from 300 K down to 10 K using an open cycle cryostat Advanced Research Systems (ARS) with helium liquid flow.

II. SAMPLE CHARACTERIZATION

The magnetite sample is a single crystal. It was characterized by transport measurements (see Fig.2 (a)). The resistance shows a first-order transition at a Verwey temperature $T_V \approx 117$ K. The sample surface with an out-of-plane direction of [110] is polished to get optical flatness. The orientation was checked by x-ray diffraction with an Empyrean diffractometer from PANalytical, using Cu-K α 1 and Cu-K α 2 radiations at ambient conditions (see Fig.2 (b)).

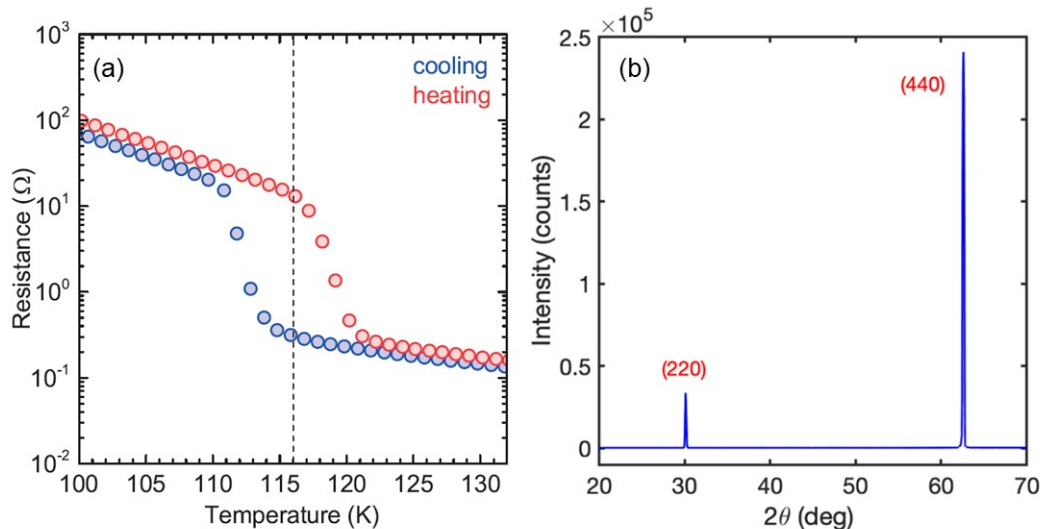


FIG. 2. (a): Temperature dependence of magnetite resistance. (b): Diffractogram of the single crystal Fe_3O_4 used in the experiment exposing the (110) surface, two sharp peaks identified as the (220) and the (440) planes give an average lattice parameter of $a = 8.3853 \text{ \AA}$ at room temperature.

III. THE ATOMIC DISPLACEMENT AND STRAIN

The atomic displacement (compression or expansion) was extracted from the Bragg peak position with the following method:

1. The atomic displacement (u) is linked to the initial atomic interplanar distance d'_{hkl} and the final atomic interplanar distance d_{hkl} by:

$$u = \frac{d'_{hkl} - d_{hkl}}{d_{hkl}}$$

2. The Bragg peak position corresponds to a specific diffraction angle θ , which is related to the interatomic distance by the Bragg law:

$$d_{hkl} = \frac{n\lambda}{2 \sin \theta}$$

$\lambda = 0.069 \text{ \AA}$ is the electron wavelength at 30 kV.

3. In our case θ varies from 0.5° to 5° , thus, in the small-angle approximation, the atomic displacement is given by:

$$u = \frac{\frac{1}{\theta'} - \frac{1}{\theta}}{\frac{1}{\theta}} = \frac{\theta - \theta'}{\theta'}$$

In this study, the electron beam goes along the $[\bar{1}\bar{1}0]$ zone axis of the crystal probing the atomic displacement along the $[110]$ direction. The different Bragg peaks visible in that configuration are presented in Fig.3. Note that the (660) peak is the most intense.

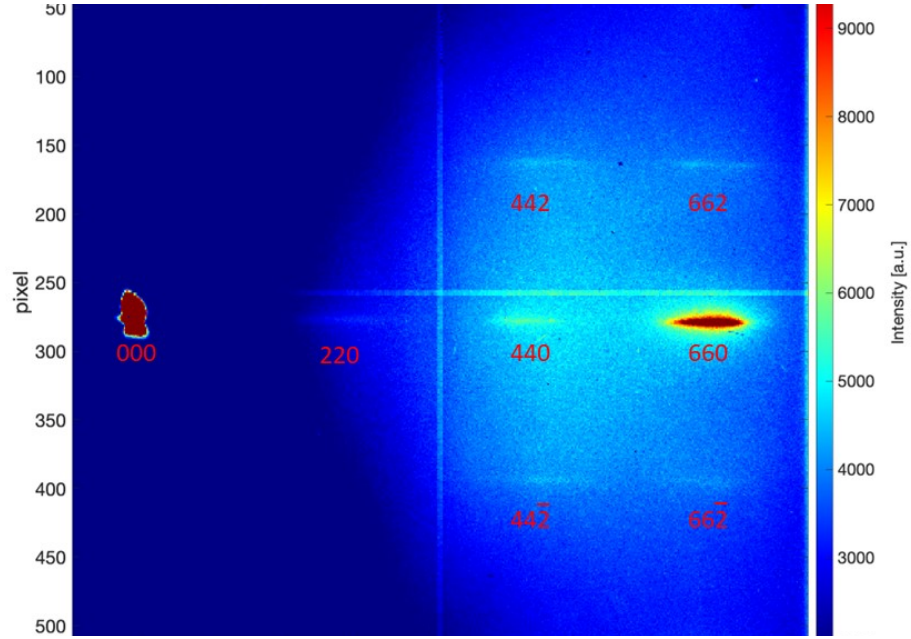


FIG. 3. Assignment of the Bragg peaks visible on our camera along the $[\bar{1}\bar{1}0]$ zone axis with 30 keV electron beam.

In the theory of elasticity, the deformation is a pure strain, which is defined by the atomic displacement (u) and the atomic position (x) [3]:

$$\varepsilon_{ij} = \frac{1}{2} \left(\frac{\partial u_i}{\partial x_j} + \frac{\partial u_j}{\partial x_i} \right)$$

The presence of strain (ε) induces a stress (σ). These two quantities are related by the elastic tensor c_{ijkl} through Hooke's law:

$$\sigma_{ij} = \sum_{kl} c_{ijkl} \varepsilon_{kl}$$

. For the cubic lattice, the elastic tensor c_{ijkl} is given by:

$$\begin{pmatrix} \sigma_{xx} \\ \sigma_{yy} \\ \sigma_{zz} \\ \sigma_{yz} \\ \sigma_{xz} \\ \sigma_{xy} \end{pmatrix} = \begin{pmatrix} c_{11} & c_{12} & c_{12} & 0 & 0 & 0 \\ c_{12} & c_{12} & c_{12} & 0 & 0 & 0 \\ c_{12} & c_{12} & c_{11} & 0 & 0 & 0 \\ 0 & 0 & 0 & c_{44} & 0 & 0 \\ 0 & 0 & 0 & 0 & c_{44} & 0 \\ 0 & 0 & 0 & 0 & 0 & c_{44} \end{pmatrix} \times \begin{pmatrix} \varepsilon_{xx} \\ \varepsilon_{yy} \\ \varepsilon_{zz} \\ 2\varepsilon_{yz} \\ 2\varepsilon_{xz} \\ 2\varepsilon_{xy} \end{pmatrix}$$

Therefore, the deformation probed along $[110]$ corresponds to ε_{xy} and the related stress σ_{xy} is:

$$\sigma_{xy} = 2c_{44}\varepsilon_{xy}$$

In the case of the monoclinic structure, the elastic tensor c_{ijkl} is:

$$\begin{pmatrix} \sigma_{xx} \\ \sigma_{yy} \\ \sigma_{zz} \\ \sigma_{yz} \\ \sigma_{xz} \\ \sigma_{xy} \end{pmatrix} = \begin{pmatrix} c_{11} & c_{12} & c_{13} & 0 & c_{15} & 0 \\ c_{12} & c_{22} & c_{23} & 0 & c_{25} & 0 \\ c_{13} & c_{23} & c_{33} & 0 & c_{35} & 0 \\ 0 & 0 & 0 & c_{44} & 0 & c_{46} \\ c_{15} & c_{25} & c_{35} & 0 & c_{55} & 0 \\ 0 & 0 & 0 & c_{46} & 0 & c_{66} \end{pmatrix} \times \begin{pmatrix} \varepsilon_{xx} \\ \varepsilon_{yy} \\ \varepsilon_{zz} \\ 2\varepsilon_{yz} \\ 2\varepsilon_{xz} \\ 2\varepsilon_{xy} \end{pmatrix}$$

Therefore, the deformation probed along [110] corresponds to ε_{xy} and the related stress σ_{xy} is:

$$\sigma_{xy} = 2(c_{46}\varepsilon_{yz} + c_{66}\varepsilon_{xy})$$

IV. GINZBURG-LANDAU ANALYSIS (SYMMETRY)

It is instructive to retrieve the symmetry of the order parameter (OP), based on the framework of Ginzburg-Landau's theory [4] and a fundamental group theory analysis. Briefly, the dominating term in the free energy F , is the linear coupling between the strain and the OP expressed as:

$$F_{coupling} = g\varepsilon\Delta$$

, where g is the coupling constant, ε is the strain, and Δ is the order parameter. The free energy coupling term is part of the total free energy and must remain invariant under all symmetry operations. In the high-temperature phase, the point group of magnetite is O_h . Consequently, the only representation in the character table (see Table.I) respecting this constrain is the A_{1g} representation. Hence, the symmetry product between ε_{xy} and Δ should belong to the A_{1g} representation (see Table.II). Since the shear strain ε_{xy} belongs to the T_{2g} representation, the order parameter Δ must belong to the T_{2g} representation as well.

O_h group	E	$8C_3$	$6C_2$	$6C_4$	$3C_2$	i	$6S_4$	$8S_6$	$3\sigma_h$	$6\sigma_d$	linear functions, rotations	quadratic functions
A_{1g}	+1	+1	+1	+1	+1	+1	+1	+1	+1	+1	-	$x^2 + y^2 + z^2$
A_{2g}	+1	+1	-1	-1	+1	+1	-1	+1	+1	-1	-	-
E_g	+2	-1	0	0	+2	+2	0	-1	+2	0	-	$(2z^2 - x^2 - y^2, x^2 - y^2)$
T_{1g}	+3	0	-1	+1	-1	+3	-1	0	-1	-1	(R_x, R_y, R_z)	-
T_{2g}	+3	0	+1	-1	-1	+3	-1	0	-1	+1	-	(xz, yz, xy)
A_{1u}	+1	+1	+1	+1	+1	-1	-1	-1	-1	-1	-	-
A_{2u}	+1	+1	-1	-1	+1	-1	+1	-1	-1	+1	-	-
E_u	+2	-1	0	0	+2	-2	0	+1	-2	0	-	-
T_{1u}	+3	0	-1	+1	-1	-3	-1	0	+1	+1	(x, y, z)	-
T_{2u}	+3	0	+1	-1	-1	-3	+1	0	+1	-1	-	-

TABLE I. Characters table for O_h point group.

	A_{1g}	A_{2g}	E_g	T_{1g}	T_{2g}	A_{1u}	A_{2u}	E_u	T_{1u}	T_{2u}
A_{1g}	A_{1g}	A_{2g}	E_g	T_{1g}	T_{2g}	A_{1u}	A_{2u}	E_u	T_{1u}	T_{2u}
A_{2g}	A_{2g}	A_{1g}	E_g	T_{2g}	T_{1g}	A_{2u}	A_{1u}	E_u	T_{2u}	T_{1u}
E_g	E_g	E_g	$A_{1g}+A_{2g}+E_g$	$T_{1g}+T_{2g}$	$T_{1g}+T_{2g}$	E_u	E_u	$A_{1u}+A_{2u}+E_u$	$T_{1u}+T_{2u}$	$T_{1u}+T_{2u}$
T_{1g}	T_{1g}	T_{2g}	$T_{1g}+T_{2g}$	$A_{1g}+E_g+T_{1g}+T_{2g}$	$A_{2g}+E_g+T_{1g}+T_{2g}$	T_{1u}	T_{2u}	$T_{1u}+T_{2u}$	$A_{1u}+E_u+T_{1u}+T_{2u}$	$A_{2u}+E_u+T_{1u}+T_{2u}$
T_{2g}	T_{2g}	T_{1g}	$T_{1g}+T_{2g}$	$A_{2g}+E_g+T_{1g}+T_{2g}$	$A_{1g}+E_g+T_{1g}+T_{2g}$	T_{2u}	T_{1u}	$T_{1u}+T_{2u}$	$A_{2u}+E_u+T_{1u}+T_{2u}$	$A_{1u}+E_u+T_{1u}+T_{2u}$
A_{1u}	A_{1u}	A_{2u}	E_u	T_{1u}	T_{2u}	A_{1g}	A_{2g}	E_g	T_{1g}	T_{2g}
A_{2u}	A_{2u}	A_{1u}	E_u	T_{2u}	T_{1u}	A_{2g}	A_{1g}	E_g	T_{2g}	T_{1g}
E_u	E_u	E_u	$A_{1u}+A_{2u}+E_u$	$T_{1u}+T_{2u}$	$T_{1u}+T_{2u}$	E_g	E_g	$A_{1g}+A_{2g}+E_g$	$T_{1g}+T_{2g}$	$T_{1g}+T_{2g}$
T_{1u}	T_{1u}	T_{2u}	$T_{1u}+T_{2u}$	$A_{1u}+E_u+T_{1u}+T_{2u}$	$A_{2u}+E_u+T_{1u}+T_{2u}$	T_{1g}	T_{2g}	$T_{1g}+T_{2g}$	$A_{1g}+E_g+T_{1g}+T_{2g}$	$A_{2g}+E_g+T_{1g}+T_{2g}$
T_{2u}	T_{2u}	T_{1u}	$T_{1u}+T_{2u}$	$A_{2u}+E_u+T_{1u}+T_{2u}$	$A_{1u}+E_u+T_{1u}+T_{2u}$	T_{2g}	T_{1g}	$T_{1g}+T_{2g}$	$A_{2g}+E_g+T_{1g}+T_{2g}$	$A_{1g}+E_g+T_{1g}+T_{2g}$

TABLE II. Product table of the O_h point group.

The T_{2g} symmetry implies that the OP contains three components:

$$\Delta = (\Delta_{xy} + \Delta_{yz} + \Delta_{xz})$$

Thus, we can rewrite the coupling free energy term as:

$$F_{coupling} = g(\varepsilon_{xy}\Delta_{xy} + \varepsilon_{yz}\Delta_{yz} + \varepsilon_{xz}\Delta_{xz})$$

Three possible scenarios follow (See Fig.4):

1. $\Delta_{xy}, \Delta_{yz}, \Delta_{xz} \implies \varepsilon_{xy}, \varepsilon_{yz}, \varepsilon_{xz} \neq 0$
Applying simultaneously three shear strains $\varepsilon_{xy}, \varepsilon_{yz}, \varepsilon_{xz}$ leads to a deviation of the angles from 90° , without any changes in the lattice parameters, $a, b,$ and c yielding a trigonal distortion (case A in Fig.4).
2. $\Delta_{xy}, \Delta_{yz} \neq 0$ and $\Delta_{xz} = 0 \implies \varepsilon_{xy}, \varepsilon_{yz} \neq 0$ and $\varepsilon_{xz} = 0$
Applying simultaneously two shear strains ε_{xy} and ε_{yz} induces the derivation of the angles from the 90° accompanied by nonequivalent lattice parameters $a \neq b \neq c$ generating a triclinic distortion (case B in Fig.4).
3. $\Delta_{yz}, \Delta_{xz} = 0$ and $\Delta_{xy} \neq 0 \implies \varepsilon_{yz}, \varepsilon_{xz} = 0$ and $\varepsilon_{xy} \neq 0$
Applying only one shear strain ε_{xy} modifies the lattice parameter c and keeps a and b equivalent, and one angle is different from 90° , leading to a monoclinic distortion (case C in Fig.4).

The latter case agrees with the low-temperature structure of magnetite Cc [5]. Hence, we conclude that the OP responsible for the structural change belongs to T_{2g} with one component $\Delta = (\Delta_{xy}, 0, 0)$.

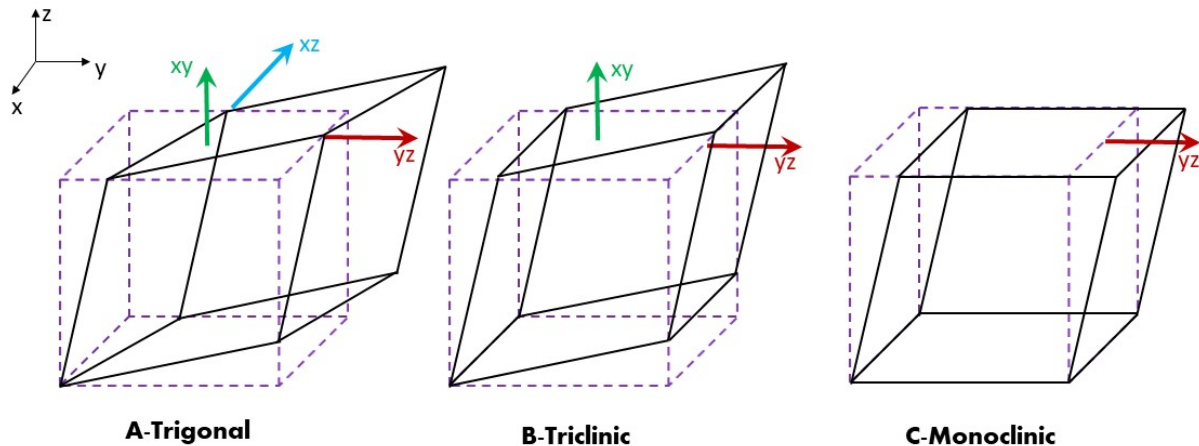


FIG. 4. The sketch of the three possible structural transformations from the cubic structure resulting from T_{2g} symmetry. The dashed purple structure corresponds to the initial cubic structure. The arrows represent the strain directions (red $=\varepsilon_{yz}$, green $=\varepsilon_{xy}$, blue $=\varepsilon_{xz}$)

V. ESTIMATION OF THE TEMPERATURE RISE

We estimate a maximum temperature rise due to energy deposited by the laser pulses with two different models, a simple heating model, and the Debye-Waller model.

1. Estimation based on the heating model

We estimate the temperature rise after the photo excitation with a simple heating model. For simplicity, we neglect heat-dissipation to assess the upper boundary and consider an ellipsoid box geometry that corresponds to the experimental condition. The model consists of solving the calorimetry equation:

$$E_{pulse} = m \int_{T_0}^{T_0 + \Delta T} C_p(T) dT$$

E_{pulse} is the energy given by a single pulse, m is the number of moles interacting retrieved from the volume considered, T is the temperature, $C_p(T)$ is the molar heat capacity, taken from ref [6] and T_0 is the initial temperature before the photoexcitation.

First, we compute the total interacting volume, which is given by the product of the beam footprint and the penetration depth. The ellipsoid beam shape is characterized with a beam profiler while the penetration depth is computed from the absorption coefficient taken from ref [7]. This gives an estimated interaction volumes of $\sim 1.87 \text{ mm} \times 0.22 \text{ mm} \times \pi \times 108 \text{ nm} = 1.4 \cdot 10^{-13} \text{ m}^3$ and $1.75 \text{ mm} \times 0.21 \text{ mm} \times \pi \times 34 \text{ nm} = 3.9 \cdot 10^{-14} \text{ m}^3$

for 800 nm and 400 nm, respectively. We finally retrieved the number of moles using 231.5 g/mol as the molar mass of Fe_3O_4 and its density of 5.17 g/cm^3 .

Next, we calculate the energy deposited by a single pulse E_{pulse} . This pulse energy is calculated as follows:

$$E_{pulse} = \frac{1 - R}{e} \frac{P}{rep.rate}$$

Where P is the total incident power, $rep.rate$ is the repetition rate of the laser (20 kHz), R the reflectivity, taken from ref [8]. Solving numerically the calorimetric equation, we find for 800 nm an increase in temperature of 46 K (58 K) for 2.9 mJ/cm^2 (3.7 mJ/cm^2). For 400 nm optical excitation the increase of temperature ΔT is equals to 60 K with 1.2 mJ/cm^2 . Note our electron probe penetration length is $\sim 5 \text{ nm}$ one order of magnitude smaller than the optical penetration length which is $\sim 34 \text{ nm}$ for the 400 nm.

2. The Debye-Waller model

To estimate the evolution of the lattice temperature after the photoexcitation, we used the Debye-Waller effect [9]. It relates how the intensity I varies as a function of the temperature-dependent atomic displacement u .

$$\frac{I_{hkl}}{I_{0hkl}} = \exp\left\{-\frac{1}{3}\langle u^2 \rangle(t) Q_{hkl}^2\right\}$$

Where, $Q_{hkl} = \frac{4\pi\theta_{hkl}}{\lambda}$ is the scattering vector and $\lambda = 0.069 \text{ \AA}$ is the electron wavelength at 30 kV.

In Fig.5 (a,b), we present the evolution of the Debye-Waller factor $\langle u^2 \rangle(t)$ after the light excitation at 800 nm and 400 nm, respectively, calculated from the evolution of the Bragg peak intensity using the following relation:

$$\langle u^2 \rangle(t) = \frac{-3 \ln\left(\frac{I_{hkl}}{I_{0hkl}}\right)}{Q_{hkl}^2}$$

To estimate the temperature T , we use the temperature variation with $\langle u^2 \rangle$ from the static data presented in Fig.6, and map the correspondence with the relation (fit):

$$T(K) = 71.628 + 50.014 \left\{ \cot\left(\frac{\langle u^2 \rangle - 0.126}{-0.0053}\right) \right\}$$

Finally, to get the temporal evolution of the estimated temperature (Fig.5(c,d)), we convert the Debye-Waller factor to temperature using the temperature variation with $\langle u^2 \rangle$ presented previously.

We found for the 800 nm optical excitation; the maximum temperature rise is $\Delta T = 111 - 89 = 22 \text{ K}$. While for the 400 nm case, the maximum temperature rise is $\Delta T = 99 - 80 = 19 \text{ K}$.

The Debye-Waller gives a temperature increase of around 20 K lower than the simple heating model. This model extracts the temperature evolution from experimental data but considers an isotropic harmonic potential and neglects other potential contributions in the intensity as the change over time of the atomic potential itself due to a structural change. Moreover, this model does not take in account the phase separation induced by the 800 nm photoexcitation.

VI. EXTENDED DELAY FOR 800 NM EXCITATION

For the 800 nm light excitation, we extended the delay up to 1.3 ns to follow the complete thermalization process. Although the atomic displacement seems to have almost completely relaxed, the intensity and the full width at half maximum (FWHM) are still far from their values before the photoexcitation.

VII. SECOND DATA SET WITH 800 NM PHOTOEXCITATION

A second data with a higher fluence (3.7 mJ/cm^2) taken with a different detector is presented in Fig.8. The comparison with the data set presented in the main text demonstrates a good consistency and that the duration and the amplitude of each stage depends on the fluence used.

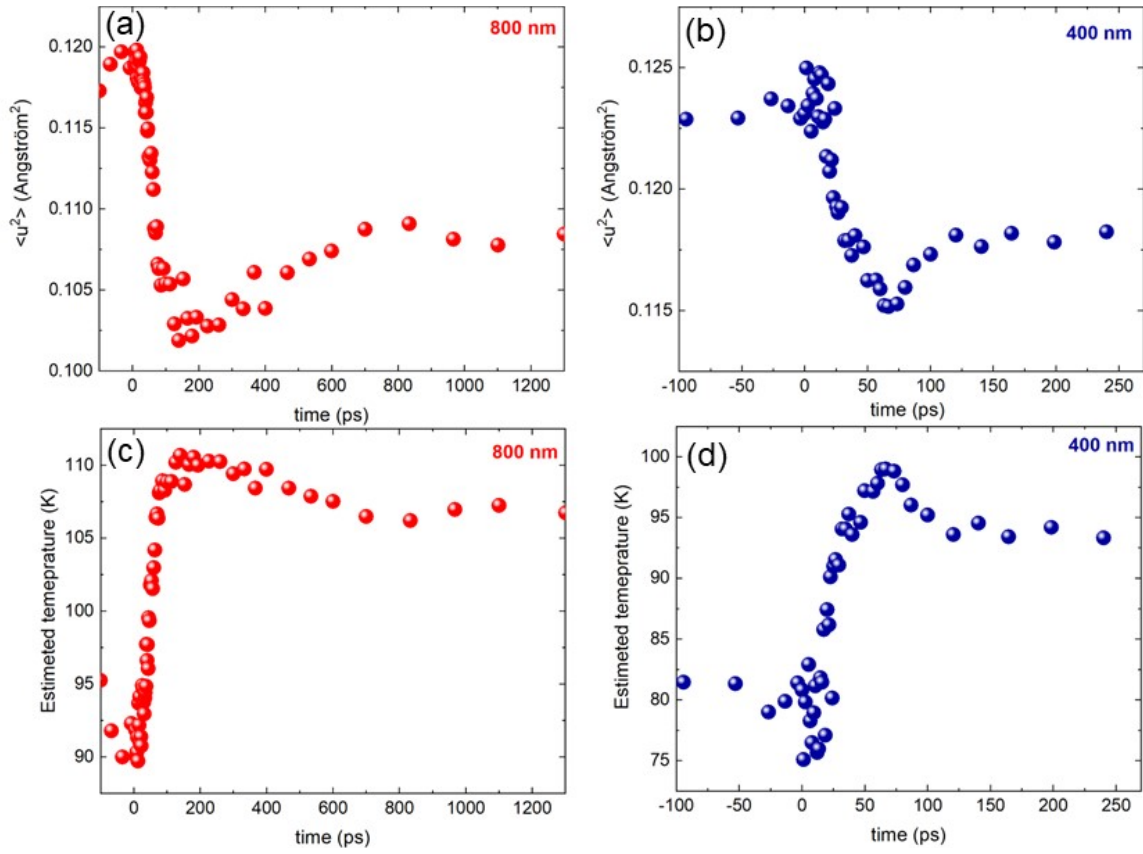


FIG. 5. (a,b): the temporal evolution of the Debye-Waller factor $\langle u^2 \rangle(t)$ for the 800 and 400 nm excitations, respectively. (c,d): the temporal evolution of the estimated temperature after light excitations 800 and 400 nm, respectively.

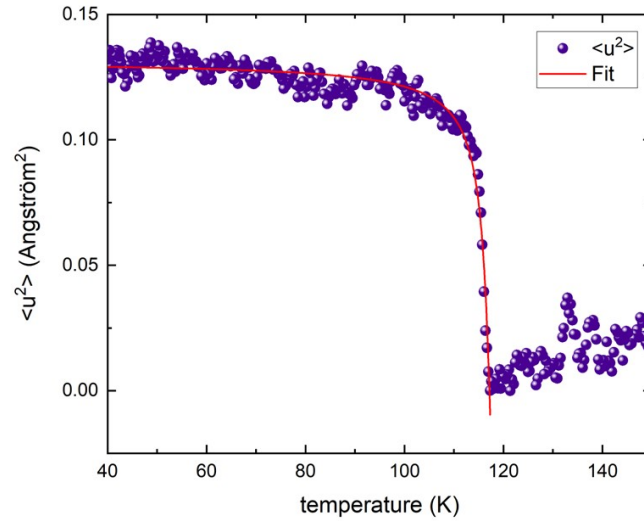


FIG. 6. The temperature dependence of the atomic displacement $\langle u^2 \rangle(t)$ extracted from the temperature dependence of the (660) Bragg peak intensity. The red line is the fit.

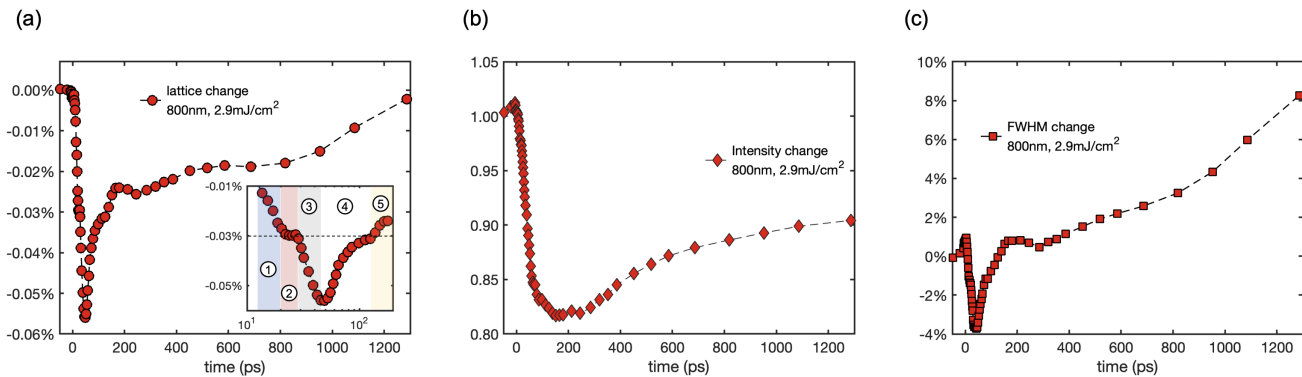


FIG. 7. (a), (b), (c) Evolution of the interplanar atomic displacement (Expansion/compression) along the [110] direction, normalized intensity and FWHM for the (660) Bragg peak under 800 nm photoexcitation, respectively.

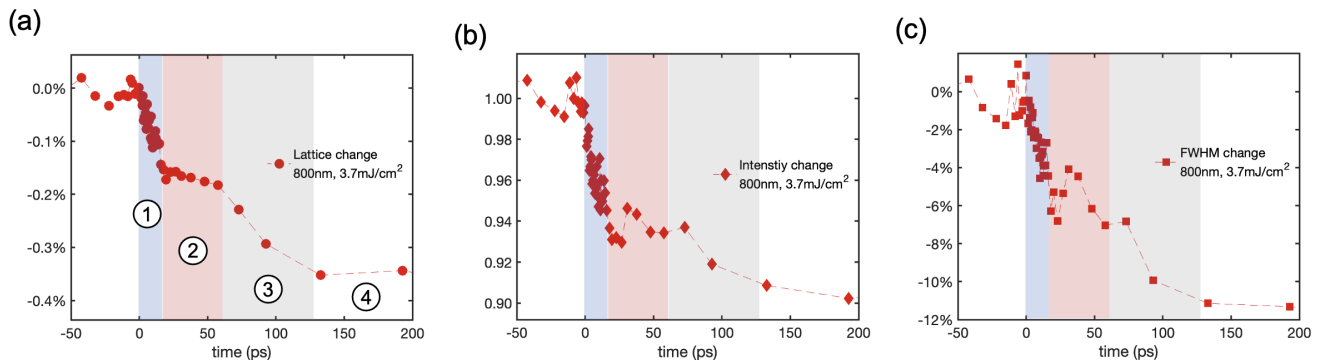


FIG. 8. (a), (b), (c) Evolution of the interplanar atomic displacement (Expansion/compression) along the [110] direction, normalized intensity and FWHM for the (660) Bragg peak under 800 nm photoexcitation, respectively. the shaded areas show the multiple compression stages.

VIII. OTHER POSSIBLE ELECTRONIC EXCITATIONS FOR THE 400 NM PHOTOEXCITATION

GGA+U calculation [10] predicts two other possible electronic excitations triggered by 400 nm light: i) the transition from an occupied t_{2g} of Fe_B^{2+} to an unoccupied e_g of Fe_B^{3+} and ii) the transition from Fe_B^{2+} to Fe_A^{3+} with an onset of approximately 2.4 eV and 2.7 eV respectively. The transition from an occupied t_{2g} of Fe_B^{2+} to an unoccupied e_g of Fe_B^{3+} leads to valency change for both Fe_B^{2+} and Fe_B^{3+} . Hence, by alternating their sites inside the trimeron unit, trimerons destruction is similar to the case of the 800 nm excitation. However, in this case, the difference is that not only the trimeron unit is destroyed but also the t_{2g} orbital ordering. Hence, we expect a compression of the lattice leading to a recovery of the cubic phase. In the second case, the transition from Fe_B^{2+} to Fe_A^{3+} leads to decreasing the number of Fe^{2+} ions and increasing Fe^{3+} at the B-sites, resulting in trimeron destruction and favoring the cubic phase. In both cases, we would expect a compression of the lattice along the [110] direction, which we did not observe in our data consistently because these two electronic excitation mechanisms are less probable than the dominant contribution provided by the O-Fe charge transfer.

IX. CONTROLLING THE MIT BY ULTRAFAST LIGHT PULSES IN MAGNETITE

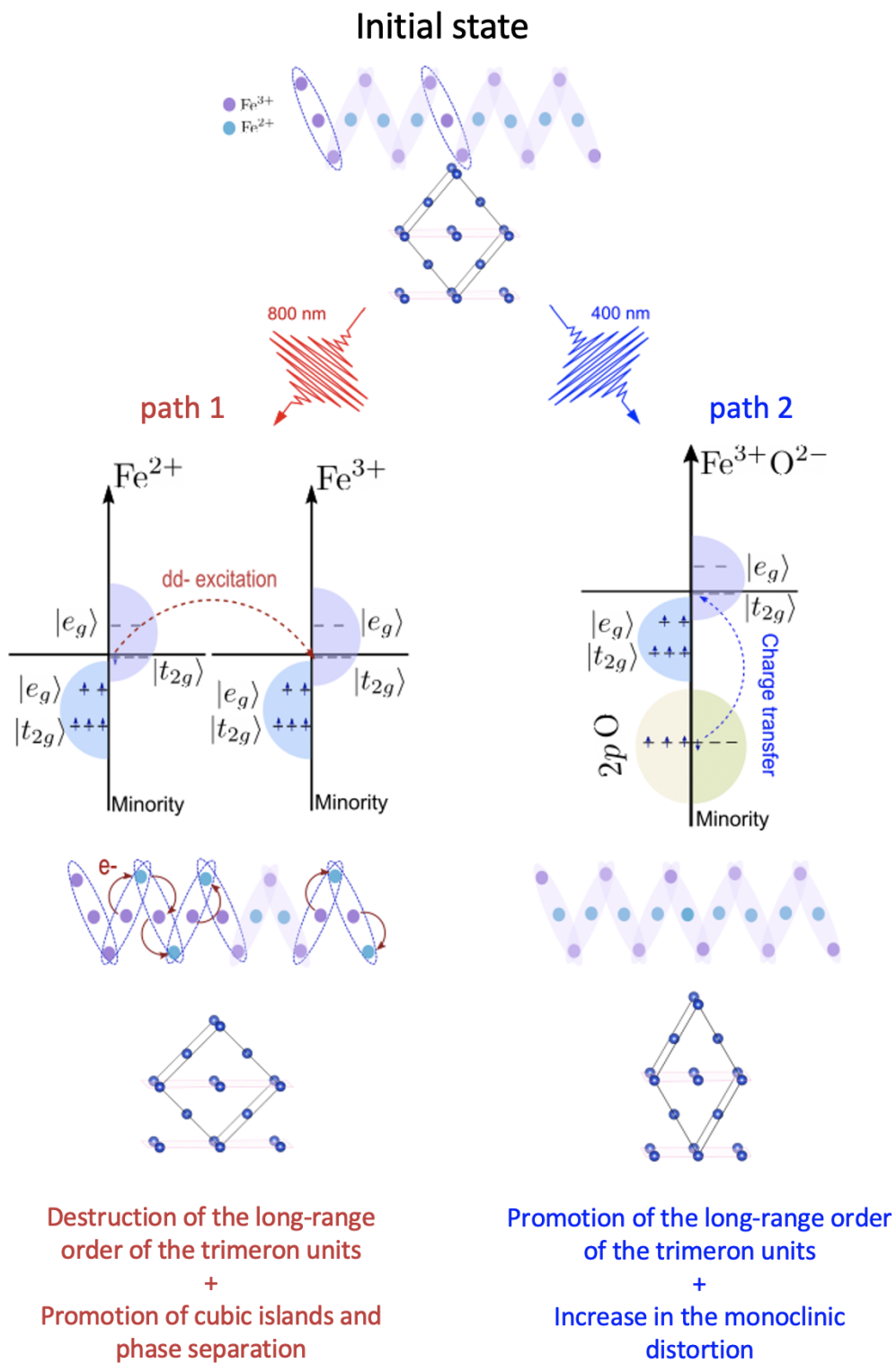


FIG. 9. A demonstrative sketch of controlling the MIT by ultrafast light pulses in magnetite. Two paths are generated from the initial state (equilibrium). Path 1 (2) corresponds to the process induced by the 800 nm (400 nm) and their effect on the electronic state, the trimerons arrangements, and the structure.

-
- [1] Giulia Fulvia Mancini, Barbara Mansart, Saverio Pagano, Bas van der Geer, Marieke de Loos, and Fabrizio Carbone. Design and implementation of a flexible beamline for fs electron diffraction experiments. *Nuclear Instruments and Methods in Physics Research Section A: Accelerators, Spectrometers, Detectors and Associated Equipment*, 691:113–122, 2012.
- [2] Francesco Pennacchio, Giovanni M. Vanacore, Giulia F. Mancini, Malte Oppermann, Rajeswari Jayaraman, Pietro Musumeci, Peter Baum, and Fabrizio Carbone. Design and implementation of an optimal laser pulse front tilting scheme for ultrafast electron diffraction in reflection geometry with high temporal resolution. *Structural Dynamics*, 4(4):044032, 2017.
- [3] B. Lüthi. Physical acoustics in the solid state. *Physical Acoustics in the Solid State*, by B. Lüthi. 426 p. 188 illus. 3-540-22910-8. Berlin: Springer, 2005., 01 2005.
- [4] L D Landau and E. M Lifschitz. *Statistical Physics*. Butterworth-Heineman, third edit edition, 1980.
- [5] M. Iizumi, T. F. Koetzle, G. Shirane, S. Chikazumi, M. Matsui, and S. Todo. Structure of magnetite (Fe₃O₄) below the Verwey transition temperature. *Acta Crystallographica Section B Structural Crystallography and Crystal Chemistry*, 38(8):2121–2133, aug 1982.
- [6] Edgar F. Westrum and Fredrik Grønvold. Magnetite (fe₃o₄) heat capacity and thermodynamic properties from 5 to 350 k, low-temperature transition. *The Journal of Chemical Thermodynamics*, 1(6):543–557, 1969.
- [7] A Schlegel, S F Alvarado, and P Wachter. Optical properties of magnetite (Fe₃O₄). *Journal of Physics C: Solid State Physics*, 12(6):1157–1164, mar 1979.
- [8] F. Randi, I. Vergara, F. Novelli, M. Esposito, M. Dell’Angela, V. A. M. Brabers, P. Metcalf, R. Kukreja, H. A. Dürr, Daniele Fausti, M. Grüninger, and F. Parmigiani. Phase separation in the nonequilibrium Verwey transition in magnetite. *Physical Review B*, 93(5):054305, feb 2016.
- [9] M. Z. Mo, V. Becker, B. K. Ofori-Okai, X. Shen, Z. Chen, B. Witte, R. Redmer, R. K. Li, M. Dunning, S. P. Weathersby, X. J. Wang, and S. H. Glenzer. Determination of the electron-lattice coupling strength of copper with ultrafast mev electron diffraction. *Review of Scientific Instruments*, 89(10):10C108, 2018.
- [10] S. Borroni, E. Baldini, V. M. Katukuri, A. Mann, K. Parlinski, D. Legut, C. Arrell, F. van Mourik, J. Teyssier, A. Kozłowski, P. Piekarczyk, O. V. Yazyev, A. M. Oleś, J. Lorenzana, and F. Carbone. Coherent generation of symmetry-forbidden phonons by light-induced electron-phonon interactions in magnetite. *Physical Review B*, 96(10):104308, sep 2017.